



Open Archive TOULOUSE Archive Ouverte (OATAO)

OATAO is an open access repository that collects the work of Toulouse researchers and makes it freely available over the web where possible.

This is an author-deposited version published in : <http://oatao.univ-toulouse.fr/>
Eprints ID : 18031

To link to this article : DOI:10.1080/00102202.2016.1214585
URL : <http://dx.doi.org/10.1080/00102202.2016.1214585>

<p>To cite this version : Pozzobon, Victor and Salvador, Sylvain and Baud, Germain and Debenest, Gérald <i>Darcy Scale Modeling of Smoldering: Impact of Heat Loss</i>. (2016) Combustion Science and Technology, vol. 189 (n° 2). pp. 340-365. ISSN 0010-2202</p>

Any correspondence concerning this service should be sent to the repository administrator: staff-oatao@listes-diff.inp-toulouse.fr

Darcy scale modelling of smouldering: impact of heat loss

Victor Pozzobon,^{*,†} Germain Baud,[†] Sylvain Salvador,[†] and Gérald Debenest^{‡,‡}

*Université de Toulouse, Mines Albi, Centre RAPSODEE, UMR CNRS 5302, 81000, Albi,
and Institut de Mécanique des Fluides de Toulouse, 31400, Toulouse*

E-mail: victor.pozzobon@mines-albi.fr

Abstract

Modelling the propagation of smoldering fronts with forced air feeding in a porous medium remains a challenge to science. One of the main difficulties is to describe the carbon oxidation reaction that supports this self-sustained process. Pore scale approaches are required to tackle this complex coupled heat and mass transfer problem with chemistry. They nevertheless require high computation effort and still miss experimental validation. Furthermore, the heat loss at the walls of the cells inherent to every laboratory scale system adds another level of complexity in the understanding of the coupling between the phenomena at stake. Indeed, it induces a non homogeneous temperature field throughout the system. In this paper, a 2D Darcy scale model is developed and validated by confrontation with experimental results from the literature, covering wide ranges of carbon content of the medium and forced air velocity. A reasonable description of the front temperature, velocity and non-consumption oxygen amount is reached. The model finally enables to bring understanding of the impact of heat loss which controls front shape and stability near the system walls.

*To whom correspondence should be addressed

[†]Université de Toulouse, Mines Albi, Centre RAPSODEE, UMR CNRS 5302

[‡]Institut de Mécanique des Fluides de Toulouse

Nomenclature

Latin symbols

- A pre exponential factor, 1/s
- c_p screen specific heat capacity, J/kg/K
- 5 C carbon mass fraction in the solid phase, -
- D mass diffusion coefficient, m²/s
- \mathbf{D} effective mass diffusion coefficient, m²/s
- d sphere diameter, m
- Ea activation energy, J/mol
- 10 fr_{CO} carbon monoxide fraction, -
- fr_{Coxi} fraction of carbon oxidized by the combustion front, -
- fr_{Ooxi} fraction of oxygen consumed by the combustion front, -
- \vec{g} acceleration due to gravity, m/s²
- H solid gas convective heat transfer coefficient, W/m²/K
- 15 h convective heat transfer coefficient, W/m²/K
- M molar mass, g/mol
- Nu Nusselt number, -
- P pressure, Pa
- Pe Péclet number, -
- 20 Pr Prandtl number, -
- Q volumic flow rate, m³/s
- \mathfrak{R} ideal gas constant, J/mol/K
- R reacting medium radius, m
- Re Reynolds number, -
- 25 S porous medium specific surface area, 1/m
- T average macroscale temperature, K
- t time, s

\vec{v} velocity, m/s

Y mass fraction, -

30 *Greek symbols*

α distribution coefficient for heat source, -

β dispersivity, m

Δh latent heat, J/kg

ϵ emissivity, -

35 ω reaction rate, kg/m³/s

λ thermal conductivity, W/m/K

λ effective thermal conductivity, W/m/K

κ permeability, m²

ρ density, kg/m³

40 σ Stefan-Boltzmann constant, W/m²/K⁴

Π reaction heat, W/m³

μ dynamic viscosity, Pa.s

τ tortuosity, -

ζ porous media porosity, -

45 *Subscripts*

Al_2O_3 alumina

bed bed

frc chemical front

g gas phase

50 i insulating material

k accounting for the different gaseous species (N₂, O₂, CO and CO₂)

L longitudinal

p pore

s solid phase

55 *sur* surrounding
T transverse
th thermal
top top of the combustion cell
Other symbol
60 $\overline{\overline{A}}$ tensors
 $\|\vec{a}\|$ vector \vec{a} norm
 ∇ nabla operator

Introduction

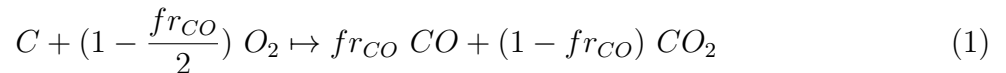
Smouldering is a process in which a combustion wave propagates through a porous medium.
65 It is involved in many situations both naturally and in man-controlled processes. Energy applications^{1,2} but also environment science^{3,4} and forest management^{5,6} are classical areas of application.

The propagation of the combustion wave is a complex problem involving heat and mass transfer together with chemical reactions and sometimes phase changes. It is admitted that
70 the energy required to enable the self-propagation of the wave is brought by the direct and flameless oxidation of some carbon in the medium. This carbon is most of the time the result of a previous solid fuel devolatilization that leads to the formation of volatile matters – gas and tars – and of a sometimes called fixed carbon. As the wave progresses, the endothermic drying of the medium is forced. If the medium contains carbonates, the
75 endothermic decarbonation of the medium occurs when the temperature overpasses 800 °C approximately⁷.

The description of these phenomena in numerical models remains a challenge to science. Theoretically, the structure of the filtration combustion front was analysed in 1D-geometry, like in the study of⁸. Several others can be found depending on the methods, but also on

80 the operating conditions, i.e., for instance cocurrent and countercurrent situations^{9,10}. In all these studies, a simplified chemistry is assumed, usually first-order and Arrhenius-like reactions. Furthermore, the strong coupling existing between heat and mass transport with a complex, multi-step chemistry, depending on local scale thermochemical conditions, is not explicitly addressed. For instance, the wave temperature depends on the amount of heat
85 released from carbon oxidation in the reacting zone. Several recent attempts have been done to study in-detail image of porous media, the dynamics and regime of such a wave at the pore scale in density variable conditions¹¹ or in non-dilatable situations¹². They clearly demonstrate, even using simplified chemistry, the competitive effect between residence time of oxygen in the front and the thermal equilibrium to maintain the combustion process.
90 Increasing the flow rate could lead to unburnt carbon and then to transition in thermal wave temperature like in¹³. In turn, the front velocity depends on a number of parameters. It is essentially governed by the stoichiometry of the carbon oxidation reaction with the fed oxygen. This nevertheless requires that the fraction of carbon actually oxidized and the fraction of oxygen actually consumed by the front - both of which depend on the front
95 temperature - are well predicted.

Also, these transitions in thermal wave transport and combustion regimes affect the chemistry. Usually, we lump all the reactions representing the carbon oxidation process into a simplified model. This has been done in¹⁴, but also in¹⁵. A global description of this very complex process can be given as:



100 Where fr_{CO} is the fraction of carbon that is oxidized into CO. The fr_{CO} parameter strongly affects the front velocity. Indeed the velocity varies by a factor of 2 when fr_{CO} changes from 0 to 1. The energy released at carbon oxidation increases from 110.5 kJ/mole for $fr_{CO} = 1$ to 393.5 kJ/mole when $fr_{CO} = 0$. This will also strongly impact the front temperature.

105 The prediction by models of the fr_{CO} value is a challenging task. This is due to the fact that final amount of CO and CO₂ observed depend on a number of parameters such as the air flow, the front temperature, the medium carbon content and the geometry of the medium particles. The primary formation of CO by the heterogeneous reaction of O₂ with solid carbon is admitted to be followed by homogeneous oxidation of CO into CO₂, but also
110 by reaction of the formed CO₂ with solid carbon. The chemical phenomena are coupled with transport phenomena that impact on gas mixing efficiency and on solid-gas contact time, as discussed in¹⁶. Therefore, predicting fr_{CO} from a numerical model can only be tackled at the pore scale. This task remains complex and a review of the possible modelling approaches is presented in¹⁷ that deals with the upscaling of such a problem from pore scale to Darcy
115 scale.

In addition to this already complex situation, another inevitable phenomenon stacks: heat loss. Indeed, no experimental device is perfectly insulated. Heat loss lowers temperature having an impact on several local physical properties such as gas density, gas viscosity and even on the fr_{CO} parameter. This adds another level of complexity in the understanding of
120 the coupling between the phenomena at stake. To summarize, the fact is that the literature does not propose a modelling approach with affordable computation time able to predict a carbon consuming front velocity and temperature, together with the amounts of unburnt carbon after the front passage and non-consumed oxygen. In addition, to our knowledge, none of the currently available models properly takes into account the heat loss. Developing
125 such a model – based on a simple description of carbon oxidation reaction - is the purpose of this paper. The global strategy is described below:

- a set of 12 experimental results was first established in a previous work¹⁸. A situation as simple as possible was aimed at, developing a model medium containing only carbon in an inert matrix of alumina. Two parameters of primary importance were varied in
130 ranges as large as possible: the carbon content between 2.30 and 3.58 % and the air flux by a factor of 10. Five experiments in extreme conditions were selected among

them.

- a numerical model was developed in this work with the aim to describe the five experiments, properly accounting for the heat loss and keeping the description of carbon oxidation reaction as simple as possible.

The final confrontation of model to experiments will be done to obtain some of the important front characteristics. These depend on the operating conditions, mainly, flow rate and carbon concentration. We will demonstrate the ability of the numerical model to explain the impact of heat loss on the smouldering front.

Experimental device and experimental database

The combustion cell used to obtain the experimental data bank is described in detail in¹⁸ (Fig. 1). Briefly, it consists of a stainless steel tube (91 mm diameter, 600 mm long) filled with a granular reactive porous medium. The tube was thermally insulated using a 50 mm thick Kaowool HS-45 insulating material, around the cylinder.

Air was fed from the top of the cell. Ignition was operated by irradiating the top of the bed with a high density radiative flux of 50 kW/m^2 , through a quartz window. Smouldering was therefore operated in the forward configuration.

The reactive porous medium was specially developed to keep the situation as simple as possible. We use porous alumina spheres with diameters ranging from 1.25 to 3.15 mm. They were enriched with solid carbon in controlled amounts thanks to a procedure described in¹⁸.

To serve as model validation benchmark, the results from five experiments were selected. In the first three experiments, the carbon content is varied from 2.30 to 3.58 % in mass. These values range from near extinction carbon content to the highest temperature the combustion cell was designed for¹⁸. In the other experiments the air flux is varied between 21 and 210 mm/s above the bed at 20 °C. One of the points is common. Table 1 summaries

the experimental conditions and main results for the selected experiments. It can be seen that the front temperature varies in a range as large as 709 °C - which is close to the known extinction temperature of 550 °C - up to 1465 °C. This last temperature is higher than
160 the maximum cell design value and was unexpected. It counter-intuitively results from the incomplete consumption of oxygen by the front. As the fed air velocity was increased by a factor of 10, the front velocity increased from 5.2 to 30.4 mm/min. The ratio of 10 is not retrieved because of the incomplete consumption of oxygen by the front at high air velocity. The experimental velocity of the front is calculated from the time separating the
165 front passage (i.e. maximum temperatures) at successive thermocouples along the cell axis. The stoichiometry of carbon consumption by the fed oxygen has been expressed by¹⁹, from which the front velocity can be expressed as a function of the experimental parameters (Eq. 2).

$$v_{frc} = \frac{v_g \rho_g}{M_g} Y_{O_2} f_{r_{O_{oxi}}} \frac{M_C}{C \rho_{bed} f_{r_{C_{oxi}}} (1 - \frac{f_{r_{CO}}}{2})} \quad (2)$$

This velocity is called theoretical front velocity in the paper, and will be used for stoichiometry checking purposes. It was shown that all of the experiments are in the reaction
170 leading mode, where the chemical front propagates faster than the thermal front. Description of such regimes and others can be found in⁸.

It was observed that all of the carbon was oxidized after the passage of the front, for all of the experiments. It was also observed in¹⁸ that the temperature at the axis of the
175 combustion cell are significantly higher than closed to the walls (1cm away from the walls). This indicates that significant heat losses occur at the cell walls. This will impact discussion on the choice of the model especially the discussion of 1D or 2D approach.

Numerical model

For the sake of simplicity and to investigate several effects, pore scale modelling was not
180 considered here. Rather, a Darcy scale approach was adopted. As a consequence and as
discussed before, it cannot be considered to predict the value of fr_{CO} from the model. Recent
studies have not lead to this prediction even in¹¹, where a complete local scale model is used.
The proposed approach here is to use in the model the values learnt from experiments, under
the form of simple functions depending only on the front temperature and on air flux. The
185 carbon combustion reaction is described globally following Eq. 1. We will describe this
reaction through an Arrhenius formulation.

The experimental results suggest that important heat losses occur at the cell walls as
pointed out before. Therefore, a 2D model was developed and not a simpler 1D model like
in¹⁵. As the insulating layer around the medium was taken into account, the model is indeed
190 expected to bring insights to explain the observed radial temperature gradients and front
curving.

The smouldering cell is described in two parts: the reaction medium and the surrounding
insulating material. The reacting porous medium is described as a homogeneous domain
governed by mass, heat and momentum conservation laws. Thermal transport equation
195 will be solved simultaneously in the insulating shell. The case was taken as a 2D transient
axisymmetrical case. A special care was put in choosing the boundary conditions which best
described experimental operating conditions (Fig. 2).

Heat balance

According to the experimental conditions, an increase in the flow rate could lead to local non
200 equilibrium²⁰. According to²¹, combustion in porous media occurs in the large range of time
and length scale. As a consequence, it usually requires local non equilibrium formulation. In
order to be as general as possible, we develop such an approach. So, heat balance is governed

by 2 equations: one for the solid phase (Eq. 3) and one for the gas phase (Eq. 6). For the solid:

$$\frac{\partial(1 - \zeta)\rho_s c_{p_s} T_s}{\partial t} = -\nabla \cdot (-(1 - \zeta)\boldsymbol{\lambda}_s \nabla T_s) + HS(T_g - T_s) + \alpha \Pi \omega \quad (3)$$

205 α is the distribution coefficient for heat source. As explained and demonstrated in²², this parameter depends on the ratio λ_s/λ_g at the pore scale. Even if the local scale geometry influences this parameter for a high value of this ratio (around 100), most of the heat (*i.e.* 99 %) is distributed to the solid phase. Π is the effective enthalpy depending on the fr_{CO} value. It is calculated as follows:

$$\Pi = (1 - fr_{CO})\Delta h_{C \rightarrow CO_2} + fr_{CO}\Delta h_{C \rightarrow CO} \quad (4)$$

210 with $\Delta h_{C \rightarrow CO_2} = 32.79 \cdot 10^6$ J/kg, $\Delta h_{C \rightarrow CO} = 9.210 \cdot 10^6$ J/kg, and ω is the chemical reaction rate expressed as:

$$\omega = Ae^{-\frac{E_a}{RT_s}} \rho_C Y_{O_2} \quad (5)$$

For the fluid phase:

$$\frac{\partial \zeta \rho_g c_{p_g} T_g}{\partial t} + \rho_g c_{p_g} \nabla \cdot (\vec{v}_g T_g) = -\nabla \cdot (-\zeta \boldsymbol{\lambda}_g \nabla T_g) - HS(T_g - T_s) + (1 - \alpha) \Pi \omega \quad (6)$$

In Eq. 3 and 6, $\boldsymbol{\lambda}_s$ and $\boldsymbol{\lambda}_g$ represent the effective conductivities of the two phases, fluid and solid. Their values depend on the local scale properties of each phase and can be estimated using classical weighted average¹⁹, for instance, or through more complex ap-
 215 proaches like upscaling procedures²³. According to²³, in non-equilibrium conditions, those properties depend on microstructure, flow and transfers at the local scale. At low thermal Péclet values, a classical conductive regime is observed with constant value of conductivities. However, increasing the Péclet values, we will observe a dispersive regime. The transition

between purely conductive and dispersive regimes depend on the microstructure but in²³,
 220 when Péclet remains under 10, the dispersive regime could be ignored.

Thermal Péclet number is a ratio between characteristic times for conduction and heat convection. It is written as follows:

$$Pe_{th} = \frac{(\rho C_p)_g \|\vec{v}_g\| d}{\lambda_g} \quad (7)$$

The thermal Péclet number values range from 2 to 20 for the largest flow rate. However, and according to the results of²³, we will not use dispersive models as only one experimental
 225 point exceeds $Pe_{th} = 10$.

The fr_{CO} parameter was described in the model as follows. The experimental results in¹⁸ reported in Table 1 showed that changing the carbon content did not impact strongly the value of fr_{CO} , and that no clear tendency could be observed. It was decided to keep a constant value of fr_{CO} of 31.4 %vol whatever the carbon content. However, fr_{CO} was
 230 observed to vary drastically with air flow variation. The values introduced in the model were 31.4, 32.1 and 23.2 %vol for the air velocities of 21, 105 and 210 mm/s respectively. Thus, fr_{CO} is considered constant throughout the medium and only depends on the flow rate at the inlet.

Several attempts in literature can be found in order to estimate from the local scale
 235 structure, the value of the heat transfer coefficient. For instance, one can find an upscaling study leading to an estimate in idealized media²³. Here, we choose to use classical correlations from the literature²⁴ (Eq. 8).

$$Nu = \frac{4H\zeta}{S\lambda_g} = 0.057 \left(\frac{4\rho_g \|\vec{v}_g\|}{S\mu_g} \right)^{0.96} Pr^{1/3} \quad (8)$$

Considering the porous media to be a bed of monodisperse, geometrical considerations lead to the following expression of the specific surface area:

$$S = \frac{6(1 - \zeta)}{d} \quad (9)$$

240 Heat transfer through the insulating shell is described using a classic heat conservation equation:

$$\frac{\partial \rho_i c_{p_i} T_i}{\partial t} = -\nabla \cdot (-\lambda_i \nabla T_i) \quad \text{in the insulating material} \quad (10)$$

The coupling between the reacting region and the insulating shell is modelled as a perfect contact. We will assume that the heat is transferred from the solid to the insulating shell. It is described by the following set of equations:

$$T_s = T_i \quad \text{on the surface between reacting medium and the insulating material} \quad (11)$$

$$-\lambda_s \nabla T_s = -\lambda_i \nabla T_i \quad \text{on the surface between reacting medium and the insulating material} \quad (12)$$

245 Finally, the boundary conditions for the insulating material with the ambient conditions are available in figure 2.

Momentum balance

Gas flow through the combustion cell was described using continuity combined with ideal gas assumption and Darcy's law in a similar way to¹⁵ or²⁵.

$$\frac{\partial \zeta \rho_g}{\partial t} + \nabla \cdot (\rho_g \vec{v}_g) = \sum_{i,g} \omega_{i,g} \quad (13)$$

250 The gas is assumed to behave as an ideal gas, thus its density can be expressed as:

$$\rho_g = \frac{P M_g}{\Re T_g} \quad (14)$$

Combining Eq. 13 and 14, we obtain Eq. 15:

$$\frac{\partial \zeta \frac{M_g}{RT_g} P}{\partial t} + \nabla \cdot (\rho_g \vec{v}_g) = (1 - fr_{CO}) \omega \frac{M_{CO_2} - M_{O_2}}{M_C} + fr_{CO} \omega \frac{M_{CO} - M_{O_2}}{2M_C} \quad (15)$$

In our case, pore Reynolds number varies from 1 to 30, depending on the flow rate. According to the general Forchheimer equation we have:

$$\nabla P = \frac{\mu}{\kappa} \vec{v}_g + \frac{\rho F}{\mu \sqrt{\kappa}} \|\vec{v}_g\| \vec{v}_g \quad (16)$$

where F is the Forchheimer coefficient accounting for inertial terms at the local scale
 255 from drag²⁶.

In a recent experimental study²⁷, the Forchheimer coefficients were obtained for various media. For spheres packing, with diameter ranging from 1 to 3 mm, F ranges between 0.43 (3 mm) to 0.54 (1 mm). Another way is to chose a unique formulation of κ depending on the Reynolds number values. According to²⁸ and in agreement with the work of²⁹ and³⁰, κ
 260 in the main flow direction can be correlated, for intermediate Re values, lesser than some hundreds, using:

$$\kappa^* = \frac{\kappa}{1 + \gamma \sqrt{Re_p}} \quad (17)$$

According to³⁰, γ value is around 0.30 for structured packing and in the case of²⁷, this varies from 0.11 to 0.14 for respectively 1 and 3 mm spheres packings. It is then possible to use:

$$\vec{v}_g = -\frac{\kappa^*}{\mu_g} \nabla (P - \rho_g \vec{g}) \quad (18)$$

265 Then, combining Eq. 15 and 18, we obtain Eq. 19:

$$\frac{\partial \frac{\zeta M_g}{\mathfrak{R}T_g} P}{\partial t} - \nabla \cdot \left(\rho_g \frac{\kappa^*}{\zeta \mu_g} \nabla (P - \rho_g \vec{g}) \right) = (1 - fr_{CO}) \omega \frac{M_{CO_2} - M_{O_2}}{M_C} + fr_{CO} \omega \frac{M_{CO} - M_{O_2}}{2M_C} \quad (19)$$

As densities and viscosities vary in space, we will obtain a non uniform field of permeability, depending on the flow regime imposed by the mass flux, but also by local thermodynamic conditions.

Mass balance

Solid carbon residue is immobile, and a classical balance equation with reaction is used:

$$\frac{\partial (1 - \zeta) \rho_C}{\partial t} = -\omega \quad (20)$$

270 At the macro scale, transport of the gaseous species is classically represented by a convection/dispersion equation:

$$\frac{\zeta \rho_g \partial Y_k}{\partial t} + \nabla \cdot (\rho_g \vec{v}_g Y_k) = \nabla \cdot (\zeta \rho_g \overline{\overline{\mathbf{D}_k^*}} \nabla Y_k) + \omega_k \quad (21)$$

With:

$$\omega_{O_2} = (1 - fr_{CO}) \omega \frac{M_{O_2}}{M_C} - fr_{CO} \omega \frac{M_{O_2}}{2M_C} \quad (22)$$

$$\omega_{CO_2} = (1 - fr_{CO}) \omega \frac{M_{CO_2}}{M_C} \quad (23)$$

$$\omega_{CO} = fr_{CO} \omega \frac{M_{CO}}{M_C} \quad (24)$$

$\overline{\overline{\mathbf{D}_k^*}}$ is a second order tensor expressed usually like:

$$\overline{\overline{D}}_k^* = \begin{pmatrix} D_T^* & 0 & 0 \\ 0 & D_T^* & 0 \\ 0 & 0 & D_L^* \end{pmatrix} \quad (25)$$

where D_L^* is the longitudinal dispersion and D_T^* the transverse dispersion coefficient. In this study, we will use classical dependence of those coefficients with the flow velocity assuming linear dispersive regime²³. We will ignore extra diagonal terms. There are classically lower than the diagonal terms up to 2 orders of magnitude²³.

$$D_L^* = \beta_L \|\vec{v}_g\| + D^* \quad (26)$$

$$D_T^* = \beta_T \|\vec{v}_g\| + D^* \quad (27)$$

Respectively, β_L and β_T are the longitudinal and transverse dispersivities.

D^* is the effective diffusion coefficient accounting for the slow down of diffusion due to the microstructure of the porous medium. According to²³, in the purely diffusive case, we obtain:

$$D^* = \frac{D}{\tau} \quad (28)$$

with a tortuosity τ fo 1.14³¹

Moreover, when dispersive regimes are linear, we obtain:

$$D_k^* = D^* I + \|\vec{v}_g\| \left(\beta_L \frac{\vec{v}_k X \vec{v}_g}{\|\vec{v}_g\|^2} + \beta_T \frac{\vec{v}_k X \vec{v}_g}{\|\vec{v}_g\|^2} \right) \quad (29)$$

with $\beta_L = d$ and $\beta_T = d/10$

Nitrogen is the diluent specie, so we impose the following constraint:

$$Y_{N_2} = 1 - Y_{O_2} - Y_{CO} - Y_{CO_2} \quad (30)$$

285 **Physical properties**

Physical properties are available in Tables 2 and 3. Because of the wide range of temperature that the model has to cover, the evolutions with temperature of several physical properties had to be taken into account (solid and gas thermal conductivities, solid and gas heat capacities, gas diffusivity and gas viscosity). Correlations coming from literature or from
290 manufacturer's data were used to describe physical property variations (alumina thermal capacity³², insulating material - manufacturer's data -³³)³⁴. Radiation inside of the porous bed was taken into account using Rossland model (Eq. 31)³⁴.

The gas phase is a mixture of nitrogen, oxygen, carbon monoxide and carbon dioxide. As air is used to feed the combustion process, nitrogen content remains high throughout
295 the combustion cell. Thus, nitrogen was taken as model gas to evaluate gas phase physical properties (thermal capacity³², thermal conductivity³⁵, dynamic viscosity³⁶).

$$\lambda_s = \lambda_{Al_2O_3} + \frac{16}{3}\zeta d\sigma T_s^3 \quad (31)$$

Equation system solving and kinetic parameters fitting

The equation system was solved using implicit sequential algorithms provided by the open source solver OpenFOAM. We use a sequential approach, solving step by step all the equa-
300 tions. We use an implicit formulation, and we use a second order numerical scheme. The kinetic parameters for the carbon oxidation reaction A and Ea where the only parameters adjusted in the model. Their value was determined to obtain the best fitting between the model predictions and all of the experimental cases considered in the work. To do so, we used 3 indicators along the cell axis were compared to experimental observations: the front
305 temperature, the front velocity and O₂ concentration remaining in the flue gas. To perform this optimisation process based on multi-objective analysis, we could use the same approach as in³⁷. However, this requires to define an objective function and then to determine the

best parameters fitted to minimize the errors. This is a dedicated study, and it is not the scope of this paper.

310 Rather, a screen was conducted in order to fit the kinetic parameters for the carbon oxidation reaction A and E_a . The starting point was the kinetic parameters proposed in¹⁸: $A = 0.327$ 1/s and $E_a = 18500$ J/mol. Yet, they yielded poor results. It is known from literature that parameters, even carefully measured, in TG experiments may have to be significantly changed in order to yield proper results in bed model³⁸. Figure 3 reports the
315 screening results. From this figure, one can see that two main areas emerge: a combustion extinguishment zone (for a given E_a , when A is too low) and a complete O_2 consumption zone (for a given E_a , when A is too high). The transition zone in between these two zones was investigated to find the best fitting values. In the end, the couple $A = 400$ 1/s and $E_a = 55500$ J/mol yielded the best results. Figure 4 shows that with the best fitting parameters
320 a prediction of the three main front characteristics is obtained over the large ranges of experimental parameters. Significant discrepancies can be observed in some cases, but it is judged that they remain acceptable considering the complexity of the smouldering process and the quite simple description adopted in the model. It is stated, at this stage, that the main objective of the work is reached here: it is possible to describe the main characteristics
325 of a smouldering front – including cases where not all of the oxygen is consumed – with a simplified description concerning the chemical reaction. We remind here that the fr_{CO} had to be given to the model; this remains the main weak point of the model.

It is interesting here to compare the identified values of A and E_a to those determined by¹⁸ in thermo-gravimetric experiments. These parameters were derived from isolated particles
330 situation in controlled temperature and oxygen surrounding. The measured activation energy was 18500 J/mol, which is approximately 3 times smaller than the value identified in the model in bed configuration. It is difficult to interpret quantitatively this difference. It can nevertheless be concluded that the simple approach consisting in measuring the kinetic parameters on a single particle and injecting them in a bed scale model is not satisfactory.

335 We use a constant activation energy like in³⁹ who showed that a constant activation energy for carbon oxidation is observed if temperature does not exceed 1650 K.

In the following section, we will focus our analysis on the coupled phenomena governing the front characteristics and discuss some results by comparison with available experimental data.

340 **Inputs of the model for comprehension of coupled phenomena**

Temperature field

Firstly, we use a set of conditions in order to establish the ability of our numerical model to capture all the physical phenomena taken into account. We will compare some experimental
345 data to the ones of the numerical model:

- the front temperature and width along the axis of the cell at 20 cm from the inlet
- radial temperatures, to see if we capture the heat losses
- temperature signal at the surface of the insulating shell

Despite the quite large diameter of the combustion cell used in the experiments, compared
350 to other works in literature, heat losses at the cell walls have a strong impact. For instance, the computed temperature field after 1 h is presented in figures 5 and 6 for the reference case, with 2.30 %C and 21 mm/s air velocity in the reactive bed, and in the insulating shell. The temperature level reaches a maximum on the axis (741°C) then radially decreases to 323°C at the inner surface of the cell. The transverse profiles exhibit the same information
355 more quantitatively (Fig. 6).

Figure 7 reports the temperature history of one thermocouple at the axis of the reacting medium. The experimentally reported history exhibits at first a plateau around 60 °C,

which is attributed to water vaporization and condensation¹⁴. Then, temperature rises until a peak value of 709 °C is reached. Afterwards, temperature decreases slowly. Numerically
360 computed temperature history - in which the water vaporization and condensation was not taken into account - shows the same trend as the experimental one. The model predicts a peak temperature of 741 °C, which is very close to monitored temperature. Agreement between numerical prediction and experimental observations appears then to be very good.

In order to check the accuracy of the 2D model, the experimental history of the thermo-
365 couples placed 1 cm away from the walls inside the reactive medium is reported in figure 8, together with the model predicted evolution. Once again, a good agreement is obtained. After 40 minutes, a rapid exponential increase of temperature is observed to reach 650 °C in several minutes. Then, a slow exponential cooling appears. Values of decay length are given in¹⁸ depending of the Péclet values. We do not reach the expected level of temperatures with
370 a difference close to 100 °C for the worst cases. Anyway, the trends are well captured. Part of the discrepancy can be explained by uncertainties in the insulating heat capacity whose maximum values of the temperature are dependent on. Perfect boundary conditions could also be questionable. We must also keep in mind that fr_{CO} is a constant in our case. A small variation of the value could lead to large increase in temperature levels, when favouring
375 CO₂ formation. This requires the determination of a complex model for fr_{CO} , depending from temperature level for instance. As we focus on determining the principal phenomena involved in the evolution of front shape, we will make the use of this simplified approach.

Capturing the temperature profile of the outer surface of the cell is a token of the quality of the heat loss through the insulating layer modelling. Both experimental observations and
380 numerical predictions are reported in figure 9. As one can see, the numerical model is able to reproduce the trends of the outer surface temperature history. The predicted outer surface temperature peak is very close to the monitored one: 55 °C for 60 °C. Thus, we can estimate that our model reproduces fairly well the thermal transport in a complex situation with multi-layered media, heterogeneous in terms of properties.

385 Based upon this, the model can be used to estimate the amount of energy lost at the
walls, compared to the heat released at carbon oxidation. The heat losses at the cell walls
were estimated by integrating the heat flux over time, all along the cell. The heat released
by carbon combustion can be calculated from the mass of carbon in the cell and the reaction
heat calculated from Eq. 4. In the reference case $Pe = 1.6$, $C = 2.3 \%$, approximately 50
390 $\%$ of the combustion energy is lost through the cell walls. This confirms the necessity of
insulating the combustion cell. Even for this quite high diameter cell - as compared to other
experimental devices used in the literature - half the energy released is lost and not left in
the gas to flow downstream.

As reported in Table 1, the agreement between the model predictions and the experi-
395 mental observations, in terms of temperature at the center of the cell, is good for all the
cases, except the highest Péclet number. The discrepancy is thought to come from the fr_{CO}
values used in the model which are constant over the medium. fr_{CO} has indeed a strong
impact on the heat released by the oxidation reaction and therefore on the temperature.
Discrepancies for the highest Péclet number case may come also from the fact that thermal
400 dispersive effects were not taken into account. In this particular case, Péclet number value
suggested that these effects may play a role on thermal behaviour of the medium. Anyway
and as a partial conclusion, our aim was to check if our model was able to capture most of
the effects involved in the combustion front propagation. We could assume that our model
is really close to the experimental reference and we could now explore make the use of it to
405 study the deformation of the front due to heat losses.

Carbon field and front shape

Using the model, we focus on 3 configurations to determine the shapes of the smouldering
front. Figure 10 reports the modelled shapes of the smouldering front in three extreme
configurations. For the reference case (placed at the center) a downward curved front is
410 observed after 10 cm, and is preserved during front propagation as illustrated at $z = 20$ cm.

The observation is similar with high air flow rate. In the case of high carbon content (left), the front is strongly curved upward; the phenomenon accentuates with the propagation. To support the interpretation of these results, figure 11 reports the amount of oxygen left in the gas downstream of the front. It can be seen that the situation can shift from total
415 consumption of oxygen to more than half the fed oxygen percolating through the front. During the experiments reported by¹⁸, such curved shapes of the fronts were observed. The curvature was sometimes upward and sometimes downward, even for fixed experimental condition such as the reference case. Understanding why a front is not flat is interesting for a man-controlled applications because it underlies the front stability question. There
420 are several reasons to explain the front shape change as already discussed in⁴⁰. The front velocity is basically controlled by the chemical reaction stoichiometry.

As long as all of the carbon is consumed and all of the fed O₂ used, the local front velocity is governed by the local axial oxygen flow rate. The local temperature can impact this flow rate in several ways. If the temperature is lower (as observed closed to the cell walls) the
425 gas density is higher and the front is faster. A low temperature also induces a smaller gas viscosity, favouring high local gas velocity and a faster front propagation.

If not all of the oxygen is consumed at the front, the front will slow down. This is likely to occur if the local temperature is low. If not all of the carbon is oxidized, the front will accelerate.

430 Sphere packings near the walls is not homogeneous as it is in the bulk of the bed; then permeability is locally increased⁴¹. This may lead to an increased gas flow rate and to a local front acceleration.

In the following, it is shown that the developed model can bring valuable understanding of the coupled phenomena governing the front shape evolution.

435 In the reference case and the high air velocity cases, the front shape is stable. This means that the different phenomena that operate to accelerate and to slow down the front at the walls are balanced. The front shape in the high carbon content experiment is not

stable: the front is faster at the walls. The potential phenomenon to slow down the front is the percolation of oxygen at the walls. Indeed, 3.5 % oxygen is predicted by the model at the walls downstream of the front, while no oxygen percolated at the cell axis. This plays a minor role as compared to front accelerating phenomena, i.e. colder temperature of the gases at the walls. It implies that:

- density and oxygen concentrations are higher at the walls
- the gas viscosity is smaller and the local gas velocity is higher

The numerical model was used to estimate the contribution of the two phenomena. This remains an indication of the possible effects of both density and viscosity on the front shape. But, in the past, this was mentioned in¹⁵, as well as channelling effects. Even if we show exhibit that heat losses is the main phenomenon explaining front curvature, they generate on the fluid properties two important effects:

- higher density at the walls, responsible for three quarters of the front deformation
- smaller gas viscosity and higher local gas velocity, responsible for one quarter of the deformation

The proportion of the importance was obtained by inhibiting turn by turn density variation at first and then, viscosity variation.

The sphere arrangement also may explain part of the faster propagation of the front at the walls. Nevertheless, the porosity increase was reported to be in a ratio of about 2 but only in a 1 particle thick zone at the walls⁴¹. We believe that this effect was negligible. Hence, it was not implemented in the model.

Furthermore, the curved shape of the front in high carbon content cases may explain the discrepancies between experimentally reported front velocities at the center of the cell and numerically predicted ones (Table 1). Indeed, the numerical model over predicts the propagation of the combustion front near the wall for these cases, meaning that oxygen is

diverted towards the cell walls. It leads to a lower oxygen flow rate at the center of the cell and therefore a lower front velocity at this location. One of the important results here is the determination of this front velocity. Using the signal obtained thanks to thermocouples, combustion front velocity could lead to a bad estimate in the case where the front is curved. We will take, at the axis, the maximum of the recorded temperatures, and then use classically this as a reference for the front location. In this study, we clearly demonstrate that this curvature is important and increases with time depending on several parameters. Determining the real front location is then subject to discussion but in Table 1, we report not the maximum of the temperatures at the axis but the location of the points, in the longitudinal direction, where 50 % of the carbon is consumed. The stoichiometry of carbon consumption by the fed oxygen has been expressed in Eq. 2 by⁴⁰.

It gives the theoretical front velocity as a function of the experimental parameters. According to¹⁸, these values range from 5 (Pe = 1.6), 19mm/min (Pe = 8) to 36.5 mm/min (Pe = 16) when carbon content is fixed at 2.3 %. The values in Table 1, for the last three cases, refer to these points. Then, one could see that our numerical model is close to the observed front temperature but also close to the theoretical ones.

Front thickness

In order to check the accuracy of our approach, we have one last indicator. This is the front thickness, depending on flow regime (Péclet number) but also on carbon content (values of temperature). It has been investigated in detail by¹⁴. The front structure was explained and the thickness of reactive zone reported using gas microsampling.

We quantify this as the distance between the positions where carbon conversion shifts from 10 % to 90 %. Table 1 reports the experimentally observed thickness's in¹⁸ and the model predicted ones. The present model appears to predict thickness's comparable to experimental ones, which can vary between 2 and 5 average particle diameters. The model also recovers the increase of the front thickness when air velocity increases. This will be

taken here just as a remark, and no particular signification will be attributed to this result.
490 Since the kinetic parameters of the carbon oxidation reaction were fitted, it is not totally surprising that the description of the front thickness has a good order of magnitude. The quite good description of a very complex pore scale problem by the present Darcy scale model may be accidental to some extent.

Conclusion

495 In this study, we develop a fully coupled heat and mass transport model in order to investigate the effects of different phenomena involved when dealing with combustion in porous media. We use a 2D Darcy scale model with a complete description of the whole phenomenology while taking into account heat losses around the reacting medium. We use a simplified chemical model based on a single oxidation reaction and a constant value of fr_{CO} . We
500 determine the kinetic parameters by minimizing the error between a set of experiments and the model predictions. The model predictions are satisfying in terms of front temperature, front velocity, and non-consumed oxygen amount over a variety of situations - with different carbon contents and air velocities, including cases in which some oxygen percolates through the front. This clearly demonstrates the ability of this tool to capture the main features
505 of the smoldering process. The remaining discrepancies were mainly attributed to the two weaknesses of the model: a constant fr_{CO} over the domain, and a very simplified description of the chemical reaction.

The model was used to bring new understanding of the effect of the heat loss on the front shape. The local cooling at the walls induces a higher gas density which is the phenomenon
510 controlling the local front shape, with only a minor contribution from the lower gas viscosity. It also enables to quantify the heat loss at the walls that are as high as half of the energy released at carbon oxidation. Accurate description of this loss is necessary to model high temperature smoldering experiments, even in a combustion cell with a diameter as high as

91 mm.

515 In this work, a very simplified description of the chemical reaction was used, but it required taking the fraction of carbon oxidized into CO from experiments. In future works, it might be envisioned to prescribe the value of fr_{CO} as a function of local thermodynamic conditions, i.e. gas velocity and temperature level.

Acknowledgement

520 The authors would like to thank the French *Agence Nationale de la Recherche* for financial support of the INSICOMB project ANR-11-BS009-005-01 in which this work was carried on. We would like to thank Bernard Auduc and Denis Marty for their technical support.

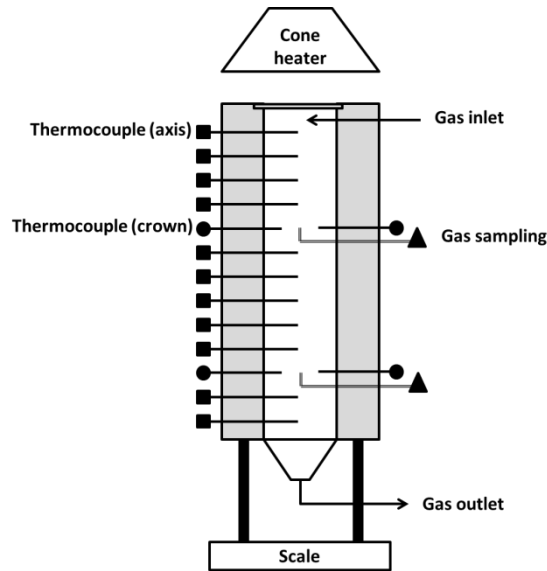


Figure 1: Schematic of the experimental apparatus¹⁸

Carbon content (%) Péclet number	← 1.6		1.6		← 1.6		1.6		← 1.6		1.6		← 1.6		1.6		← 1.6		1.6		
	Exp.	Num.	Exp.	Num.	Exp.	Num.	Exp.	Num.	Exp.	Num.	Exp.	Num.	Exp.	Num.	Exp.	Num.	Exp.	Num.	Exp.	Num.	
Peak temperature (°C)	1173	1259	1066	1123	709	740	1056	983	1465	1151											
Front velocity (mm/min)	5.3	4.5	5.7	4.9	5.2	5.0	17.0	17.4	31.3	33.0											
Remaining oxygen (absolute %vol)	0.3	0	0.5	0	5.5	4.3	11.4	9.3	11.3	9.7											
f_{rCO} (%vol)	33.2	31.4	25.7	31.4	35.5	31.4	32.1	32.1	23.2	23.2											
Air velocity at 20 °C (mm/s)	21	21	21	21	21	21	105	105	210	210											
Consumed carbon (%)	100	100	100	100	100	100	100	100	100	100											
Front thickness (mm)	4	3	4	4	4	6	8	6	10	10											

Table 1: Experimental observations and numerical predictions

Symbol	Name	Value	Dimension	Reference
$\lambda_{Al_2O_3}$	Alumina thermal conductivity	0.447	W/m/K	Measured
ρ_s	Sphere density	1475	kg/m ³	Measured
ζ	Porosity	0.452	-	Measured
κ	Permeability	2.809 10 ⁻⁹	m ²	Estimated with Kozeny Carman law
τ	Tortuosity	1.14	-	³¹
S	Specific surface area	1644	1/m	Estimated
d	Average sphere diameter	2 10 ⁻³	m	Measured
R	Reacting medium diameter	91 10 ⁻³	m	Measured
ϵ_s	Emissivity	0.5	-	Estimated
T_{sur}	Surrounding temperature	293	K	Measured

Table 2: Reacting medium physical properties

Symbol	Name	Value	Dimension	Reference
ρ_i	Density	673	kg/m ³	Measured
h_i	Convective heat transfer coefficient	10	W/m ² /K	Estimated as free convection
ϵ_i	Emissivity	0.1	-	Estimated

Table 3: Insulating material physical properties

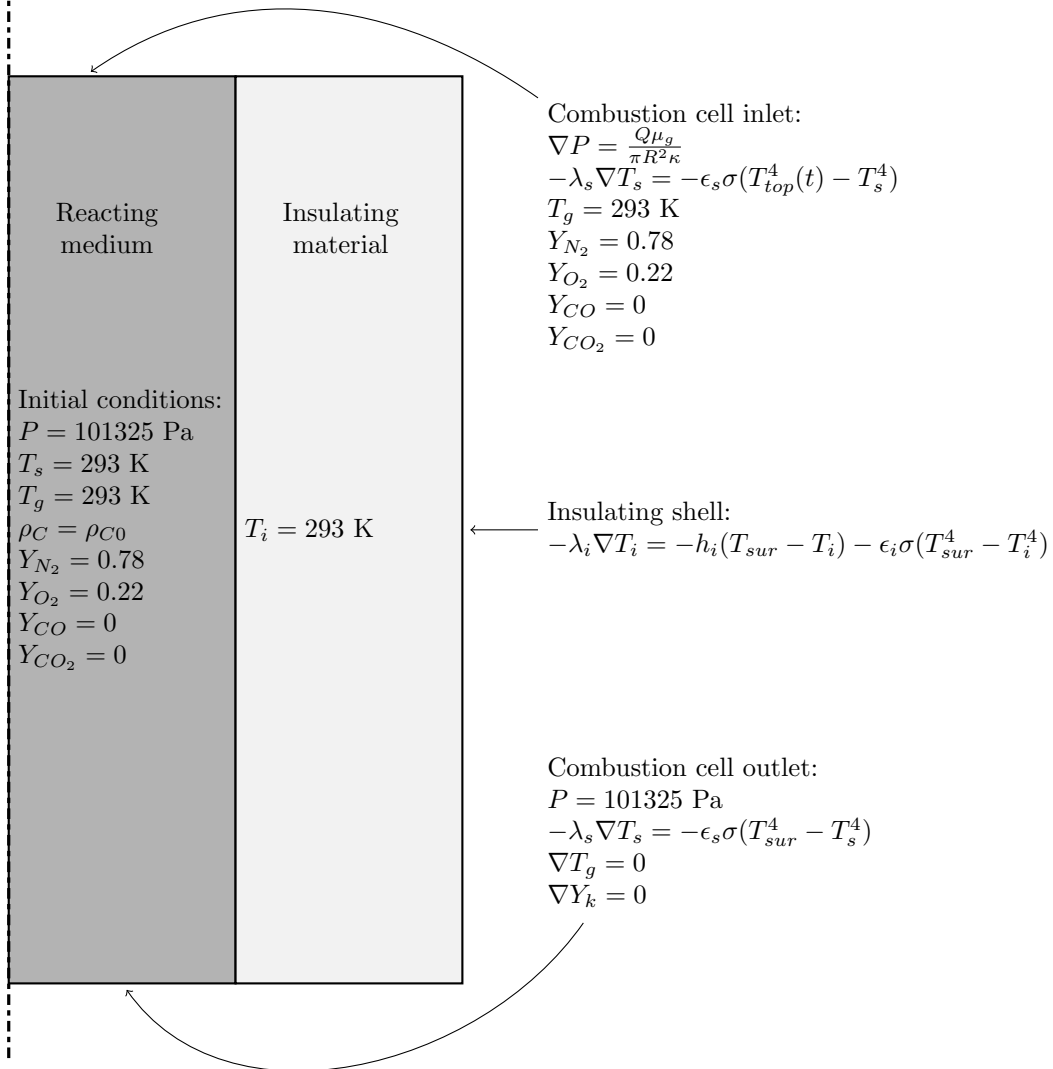


Figure 2: Numerical domain schematic with boundary conditions

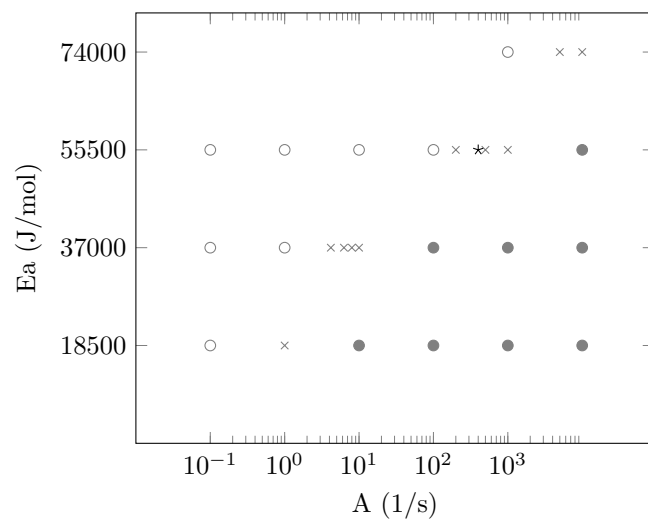
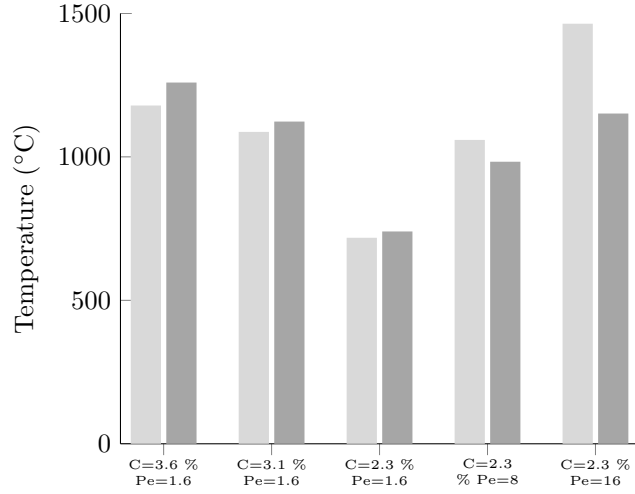
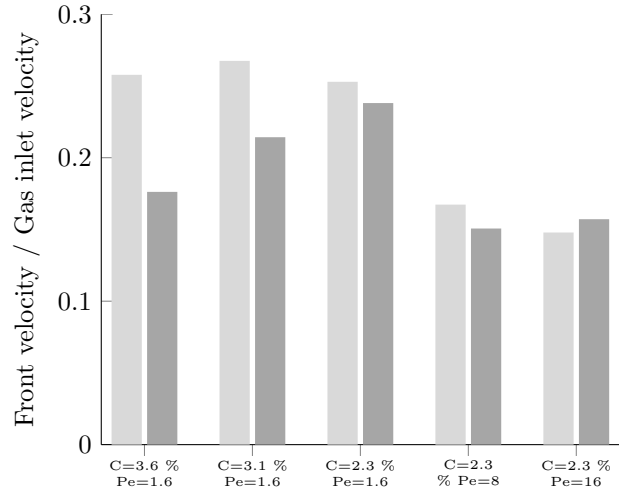


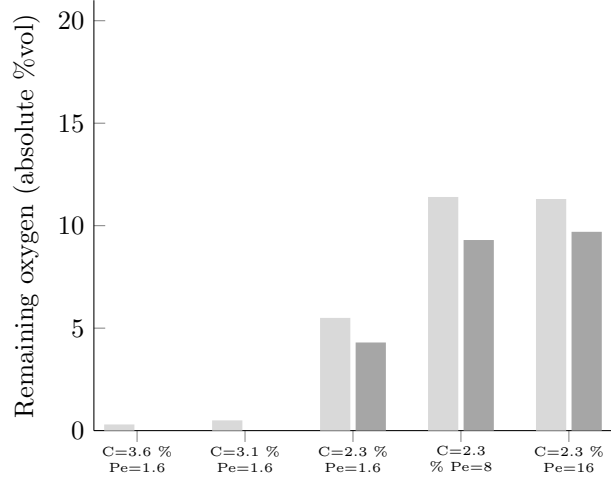
Figure 3: Screening for A and Ea. Open circle: combustion extinction, closed circle: complete oxygen consumption, cross: potential values, star: best fitting values



(a) Core temperature



(b) Chemical front velocity



(c) Remaining oxygen after the front

Figure 4: Experimental observation and numerical predictions. Light gray: experimental observations, dark gray: numerical predictions

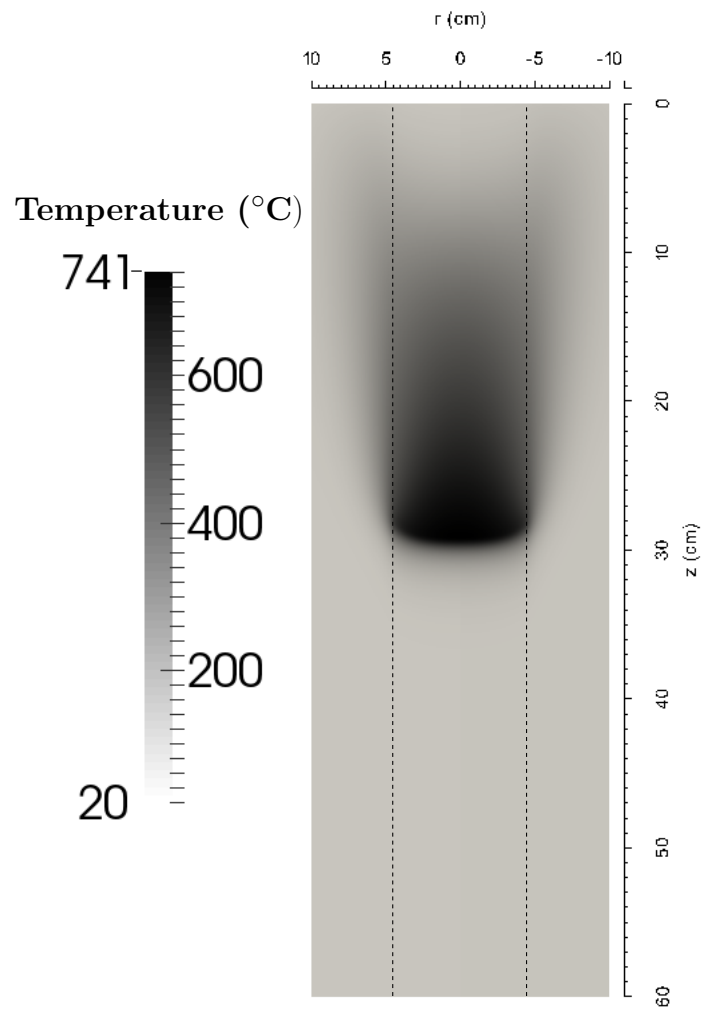


Figure 5: Temperature field inside of the combustion cell after 1 h. $C = 2.3 \%$, $Pe = 1.6$

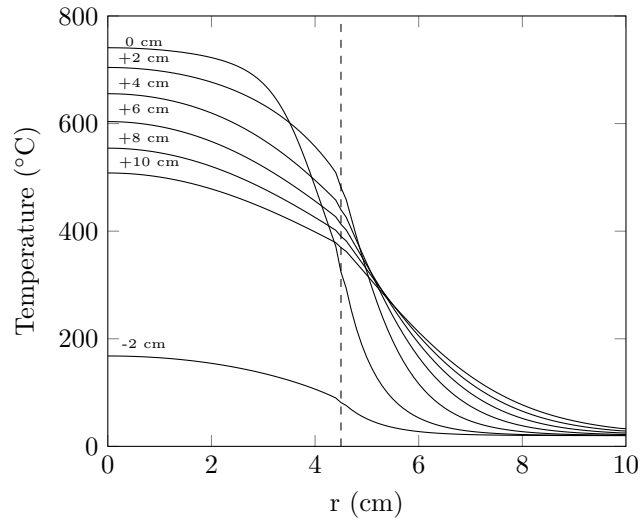


Figure 6: Temperature profiles after 1 h at various locations relative to the front. Front position: 31 cm. $C = 2.3 \%$, $Pe = 1.6$

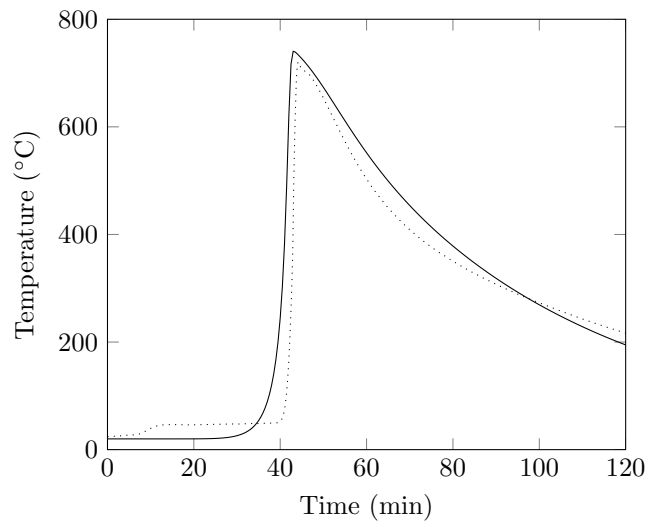


Figure 7: Temperature history on the revolution axis at 19 cm from the inlet. Continuous line: model, dotted line: experimental observations. $C = 2.3 \%$, $Pe = 1.6$

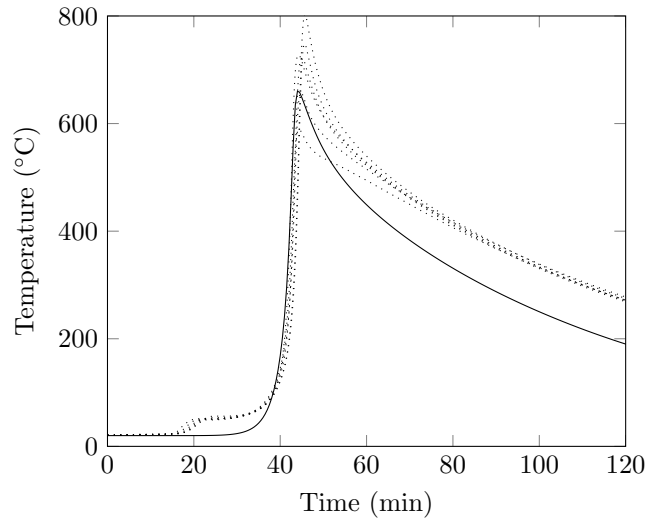


Figure 8: Temperature history 1 cm away from the wall at 19 cm from the inlet. Continuous line: model, dotted line: experimental observations. $C = 2.3 \%$, $Pe = 1.6$

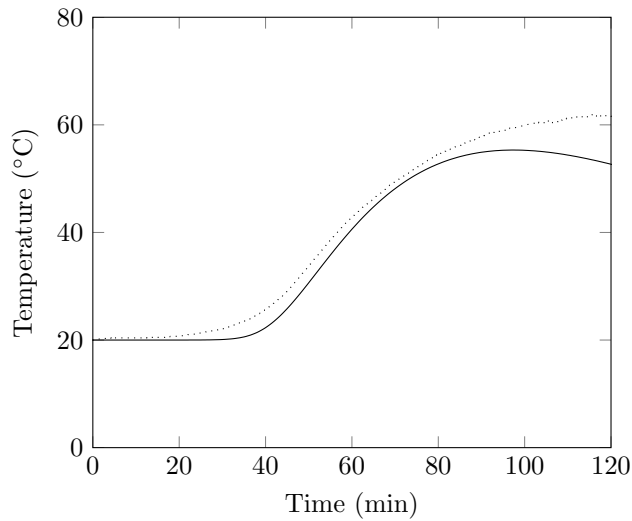


Figure 9: Superimposition of the temperature histories on outer surface of the cell at 19 cm from the inlet. Continuous line: model, dotted line: experimental observations

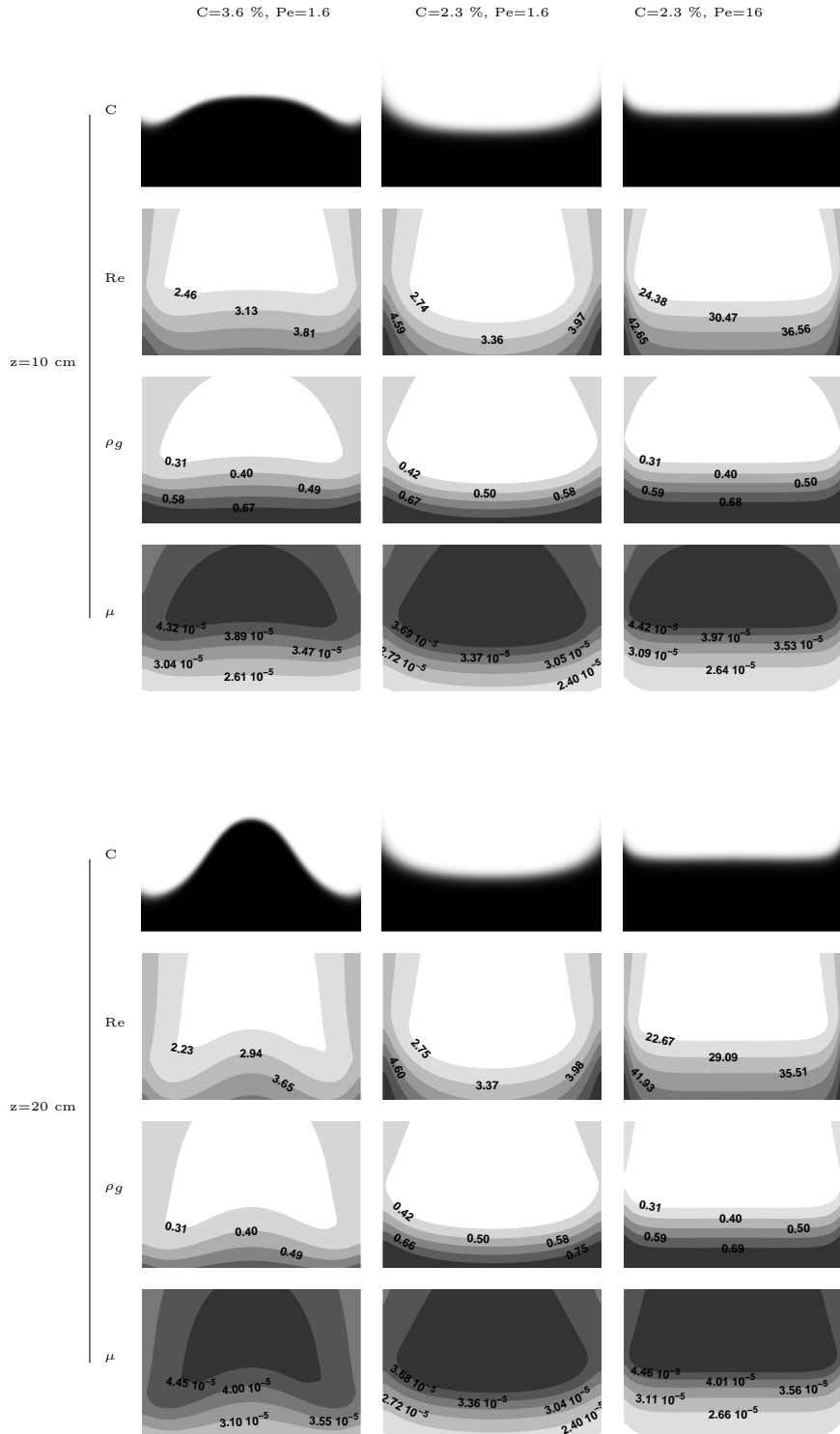


Figure 10: Different fronts shapes, viscosity, density and Reynolds number maps observed in the reference case (center), with high carbon content (left) and with high gas velocity (right). Color legend: the darker, the higher

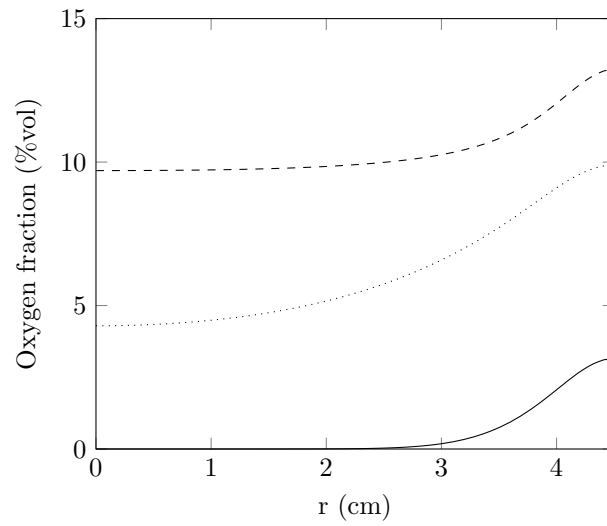


Figure 11: Remaining oxygen downstream of the front. Continuous line: $C = 3.6\%$, $Pe = 1.6$, dotted line (reference case): $C = 2.3\%$, $Pe = 1.6$, dashed line: $C = 2.3\%$, $Pe = 16$

References

- (1) Akkutlu, I. Y.; Yortsos, Y. C. *Combustion and Flame* **2003**, *134*, 229–247.
- 525 (2) Mailybaev, A. A.; Bruining, J.; Marchesin, D. *Combustion and Flame* **2011**, *158*, 1097–1108.
- (3) Vantelon, J.-P.; Lodeho, B.; Pignoux, S.; Ellzey, J. L.; Torero, J. L. *Proceedings of the Combustion Institute* **2005**, *30*, 2239–2246.
- (4) Pironi, P.; Switzer, C.; Rein, G.; Fuentes, A.; Gerhard, J. I.; Torero, J. L. *Proceedings of the Combustion Institute* **2009**, *32*, 1957–1964.
- 530 (5) Rein, G.; Cleaver, N.; Ashton, C.; Pironi, P.; Torero, J. L. *CATENA* **2008**, *74*, 304–309.
- (6) Page, S. E.; Siegert, F.; Rieley, J. O.; Boehm, H.-D. V.; Jaya, A.; Limin, S. *Nature* **2002**, *420*, 61–65.
- (7) Sennoune, M.; Salvador, S.; Debenest, G. *Energy & Fuels* **2011**, *26*, 391–399.
- 535 (8) Aldushin, A. P.; Septyarskii, B. S.; Shkadinskii, K. G. *Combustion, Explosion and Shock Waves* **1980**, *16*, 33–40.
- (9) Schult, D.; Matkowsky, B.; Volpert, V.; Fernandezpello, A. *Combustion and Flame* **1995**, *101*, 471–490, WOS:A1995RA12600008.
- (10) Schult, D. A.; Bayliss, A.; Matkowsky, B. J. *Siam Journal on Applied Mathematics* **1998**, *58*, 806–852, WOS:000072695600006.
- 540 (11) Yang, C.; Debenest, G. *Combustion Science and Technology* **2014**, *186*, 1954–1974.
- (12) Debenest, G.; Mourzenko, V. V.; Thovert, J. F. *Combustion Theory and Modelling* **2005**, *9*, 301–321.
- (13) Elayeb, M. *Modélisation à l'échelle microscopique de transports avec réaction en milieu poreux: combustion en lit fixe*; 2008.
- 545

- (14) Martins, M. F.; Salvador, S.; Thovert, J.-F.; Debenest, G. *Fuel* **2010**, *89*, 133–143, WOS:000271295000017.
- (15) Fadaei, H.; Sennoune, M.; Salvador, S.; Lapene, A.; Debenest, G. *Fuel* **2012**, *95*, 197–205, WOS:000300615900026.
- 550 (16) Zajdlik, R.; Jelemensky, L.; Remiarova, B.; Markos, J. *Chemical Engineering Science* **2001**, *56*, 1355–1361, WOS:000167819200017.
- (17) Yang, C.; Thovert, J.-F.; Debenest, G. *International Journal of Heat and Mass Transfer* **2015**, *84*, 862–875.
- (18) Germain Baud, S. S. *Energy & Fuels* **2015**, *29*.
- 555 (19) Kansa, E.; Perlee, H.; Chaiken, R. *Combustion and Flame* **1977**, *29*, 311–324, WOS:A1977DU60400010.
- (20) Debenest, G.; Mourzenko, V. V.; Thovert, J.-F. *Combustion Science and Technology* **2008**, *180*, 2170–2185, WOS:000260228100005.
- (21) Oliveira, A. A. M.; Kaviany, M. *Progress in Energy and Combustion Science* **2001**, *27*,
560 523–545.
- (22) Michel Quintard, B. L. *Symposium on Energy Engineering in the 21st Century, Begell House, New York* **2000**, *2*, 482–489.
- (23) Quintard, M.; Kaviany, M.; Whitaker, S. *Advances in Water Resources* **1997**, *20*, 77–94.
- (24) Geb, D.; Zhou, F.; Catton, I. *Journal of Heat Transfer* **2012**, *134*, 042604–042604.
- 565 (25) Lapene, A.; Debenest, G.; Quintard, M.; Martins, M.; Salvador, S. *IREME* **2008**, *12*.
- (26) Bejan, A. *Convective Heat Transfer*; 1984.

- (27) Dukhan, N.; Bağcı, Ö.; Özdemir, M. *Experimental Thermal and Fluid Science* **2014**, *57*, 425–433.
- (28) Chauveteau, G.; Thirriot, C. *Sur les pertes de charge en écoulement laminaire dans quelques géométries simple et dans le milieu poreux.*, trieste ed.; 1965.
- (29) Skjetne, E.; Auriault, J.-L. *Transport in Porous Media* **1999**, *36*, 131–147.
- (30) Soulaine, C.; Quintard, M. *International Journal of Heat and Mass Transfer* **2014**, *74*, 88–100.
- (31) Sobieski, W.; Zhang, Q.; Liu, C. *Transport in Porous Media* **2012**, *93*, 431–451.
- (32) Chase, M. W.; United States,; National Bureau of Standards, *NIST-JANAF Thermochemical Tables*, fourth edition ed.; American Chemical Society ; American Institute of Physics for the National Bureau of Standards: Washington, D.C.; New York, 1998.
- (33) Ceramics, T. *Organic RCF Vacuum Formed Products*.
- (34) Chen, J. C.; Churchill, S. W. *AIChE Journal* **1963**, *9*, 35–41.
- (35) Zimina, N. *Teplofiz. Vys. Temp* **1964**, 869–878.
- (36) Gupta, M.; Yang, J.; Roy, C. *Fuel* **2003**, *82*, 919–927, WOS:000182003900006.
- (37) Lapene, A.; Debenest, G.; Quintard, M.; Castanier, L. M.; Gerritsen, M. G.; Kavscek, A. R. *Energy & Fuels* **2015**, *29*, 1119–1129.
- (38) Teixeira, G.; Salvador, S.; Van de Steene, L. Gazéification de charbon de granules de bois : comportement thermochimique et mécanique d'un lit fixe continu. Ph.D. thesis, INP Toulouse, Toulouse, 2012.
- (39) Field, M.; Gill, D.; Morgan, B.; Hawksley, P. *British Coam Utilizatioon Research Association* **1967**, 155–173.

- (40) Sennoune, M.; Salvador, S.; Debenest, G. *Energy & Fuels* **2012**, *26*, 391–399,
WOS:000299583400042.
- (41) White, S. M.; Tien, P. C. L. *Wärme - und Stoffübertragung* **1987**, *21*, 291–296.